J. Fluid Mech. (2024), *vol*. 997, A34, doi:10.1017/jfm.2024.783

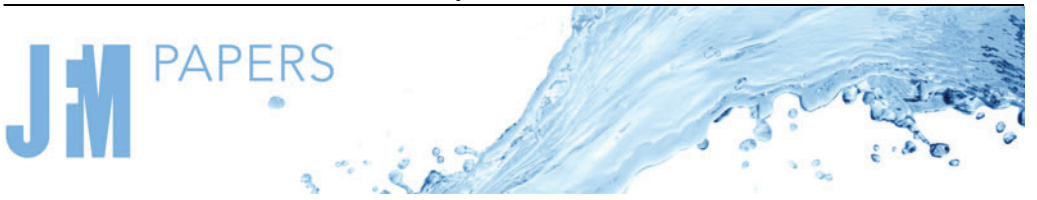

Zigzag instability of columnar Taylor–Green vortices in a strongly stratified fluid

Junwei Guo[1], **John R. Taylor**[2] **and Qi Zhou**[1],†

[1]Department of Civil Engineering, University of Calgary, Calgary, Alberta T2N 1N4, Canada

[2]Department of Applied Mathematics and Theoretical Physics, Centre for Mathematical Sciences, University of Cambridge, Wilberforce Road, Cambridge CB3 0WA, UK

(Received 10 April 2024; revised 19 June 2024; accepted 8 July 2024)

We investigate the dynamics of a columnar Taylor–Green vortex array under strong stratification, focusing on Froude numbers $0.125 \leq Fr \leq 1.0$, with the aim of identifying and understanding the primary instabilities that lead to the vortices' breakdown. Linear stability analysis reveals that the fastest-growing vertical wavenumber scales with Fr^{-1}, while the dimensionless growth rate remains approximately constant. The most unstable eigenmode, identified as the mixed hyperbolic mode by Hattori *et al.* (*J. Fluid Mech.*, vol. 909, 2021, A4), bears significant similarities to the zigzag instability, first discovered by Billant & Chomaz (*J. Fluid Mech.*, vol. 418, 2000, pp. 167–188). Direct numerical simulations further confirm that the zigzag instability is crucial in amplifying initial random perturbations to finite amplitude, with the flow structure and modal growth rate consistent with the linear stability analysis. In particular, the characteristic vertical length scale of turbulence matches that of the fastest-growing linear mode. These findings underscore the broader relevance of the zigzag instability mechanism beyond its initial discovery in vortex pairs, demonstrating its role in facilitating direct energy transfer from vertically uniform vortical motions to a characteristic vertical length scale proportional to Fr in strongly stratified flows.

Key words: vortex instability, stratified turbulence, transition to turbulence

1. Introduction

Columnar vortices can be viewed as an idealization of the structure generated by horizontal shear in geophysical settings, for example, the vortex street forming behind an island in the atmosphere (see e.g. Potylitsin & Peltier 1998; Spedding 2014). In density-stratified flow experiments, turbulence generation often involves external stirring with a set of vertical bars (e.g. Holford & Linden 1999), leading to vortex columns with pronounced vertical

† Email address for correspondence: qi.zhou1@ucalgary.ca

vorticity (Praud, Fincham & Sommeria 2005), which may become unstable and lead to turbulence. Numerical simulations often adopt a similar approach for energy injection into a stratified flow system, where turbulence is sustained by forcing the vertically uniform vortical modes (e.g. Waite & Bartello 2004; Brethouwer *et al.* 2007; Howland, Taylor & Caulfield 2020). The instabilities of such vertically uniform vortical motions are considered to provide an important link in the downscale energy transfer within strongly stratified turbulent flows (Augier, Chomaz & Billant 2012; Waite 2013).

One particular route for this energy pathway from (large) horizontal scales characterizing columnar vortices to (small) vertical scales influenced by buoyancy is the zigzag instability, first discovered by Billant & Chomaz (2000*a*,*b*,*c*). A distinguishing feature of this instability is that the most unstable vertical wavelength scales with U_0/N, while the corresponding growth rate scales with U_0/L. Here, U_0 and L are the characteristic horizontal velocity and length scale, respectively, and N is the buoyancy frequency. Billant and Chomaz demonstrated how a columnar vortex pair (or a dipole), initially uniform in the vertical direction, would undergo a sinusoidal deformation that self-amplifies and results in the vortex dipole's breakdown. Direct numerical simulations (DNS) studies of the zigzag instability have been focused on a pair of vortices (Otheguy, Chomaz & Billant 2006; Deloncle, Billant & Chomaz 2008; Waite & Smolarkiewicz 2008; Augier & Billant 2011; Augier *et al.* 2012), with the notable exception of Deloncle, Billant & Chomaz (2011), who investigated an array of vortices where the spacing between the vortices is much larger than the vortex size.

In the present study, we focus on a configuration featuring a two-by-two array of columnar vortices. The base flow, which can be considered as a vertically uniform variant of the flow first investigated by Taylor & Green (1937), is visualized in figure 1. The stability properties of various types of columnar vortex arrays have been studied for density-stratified and/or rotating fluids (Dritschel & de la Torre Juárez 1996; Potylitsin & Peltier 1998; Deloncle *et al.* 2011; Suzuki, Hirota & Hattori 2018; Hattori *et al.* 2021; Hattori & Hirota 2023). Suzuki *et al.* (2018) considered two-dimensional (2-D) Taylor–Green (TG) vortices under stable stratification, highlighting the role of hyperbolic stagnation points in the instabilities of vortex arrays. They introduced a class of instabilities termed 'strato-hyperbolic' (SH), resulting from the interaction of hyperbolic instabilities in non-stratified TG vortices (see e.g. Leblanc & Godeferd 1999) with internal gravity waves being phase-shifted near the hyperbolic stagnation points. More recently, Hattori *et al.* (2021) identified additional instability types within the TG vortex array, including a novel 'mixed hyperbolic' (MH) instability. Hattori & Hirota (2023) further incorporated the effects of rotation in their stability analysis.

Despite being considered a generic mechanism (Billant & Chomaz 2000*c*), the zigzag instability has yet to be identified in the context of a columnar vortex array, except in cases where the vortices are well separated from each other (Deloncle *et al.* 2011). Suzuki *et al.* (2018) made a comparison between the zigzag and SH instabilities, describing the latter as a 'short-wave' instability for which the vertical wavelength and the horizontal scale of the vortices are comparable. In contrast, the zigzag instability was considered by Suzuki *et al.* (2018) as a 'long-wave' instability with wavelengths larger than the size of the vortices, although the authors also stated that this wavelength could decrease with strong stratification. Our paper will demonstrate that the instabilities in a columnar vortex array can indeed be short-wave. Hattori & Hirota (2023) contrasted the instabilities observed in TG vortices with those in the vortex array scenario investigated by Deloncle *et al.* (2011), noting that zigzag instability is more likely in the latter configuration due to the relatively large spacing between the vortices. They suggest that the absence of zigzag instability in

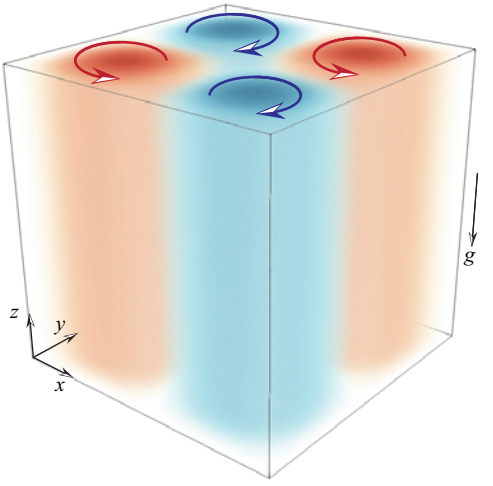

Figure 1. Visualization of columnar Taylor–Green vortices, i.e. the base flow described by (2.7). Colour illustrates the vertical vorticity $\Omega_z \equiv \partial_x V - \partial_y U$.

TG vortices could be attributed to the 'strong symmetry' enforced by the periodicity over the horizontal plane.

When stratification is strong, i.e. when the Froude number (Fr) is order 1 or below, Hattori *et al.* (2021) showed that the MH instability tends to produce the most unstable mode across all vertical wavenumbers. The MH modes were shown to have vortical structures that are different from the SH modes. The fastest-growing wavenumber in MH modes, k_{fgm}, is smaller than in SH modes, and k_{fgm} increases as Fr decreases for MH modes, which is reminiscent of the scaling expected of zigzag instabilities. Hattori *et al.* (2021) did not describe the physical mechanism associated with the growth of MH modes. The possible connection between MH modes and zigzag instability also remains unclear. To our knowledge, there have been no detailed studies of the MH modes beyond the linear stability analysis by Hattori *et al.* (2021), and their exact role in the breakdown of columnar vortex arrays warrants further investigation.

In this paper, we examine the stability properties of columnar TG vortices using both linear stability analysis and DNS, with the main aim of understanding the primary instability of such a vortex array. We focus on $Fr \leq 1$, for which the stratification is strong enough such that the most unstable wavelength of the primary instability, as we will show, follows the buoyancy scaling of U_0/N (Billant & Chomaz 2001). In § 2, we present the linear stability analysis, elucidate the instability mechanism of the unstable linear eigenmodes, and discuss connections with the zigzag instability. In § 3, we use fully nonlinear simulations to validate whether the linear instability identified in § 2 is indeed dynamically relevant in the breakdown of the TG vortices. Concluding remarks are offered in § 4.

2. Linear stability analysis

2.1. *Formulation*

The incompressible Navier–Stokes equations under the Boussinesq approximation are expressed in dimensional form as

$$\frac{\partial \boldsymbol{u}^*}{\partial t^*} + \boldsymbol{u}^* \cdot \boldsymbol{\nabla}^* \boldsymbol{u}^* = -\frac{1}{\rho_0} \boldsymbol{\nabla}^* \Pi^* + \nu \, \boldsymbol{\nabla}^{*2} \boldsymbol{u}^* + \frac{\rho^*}{\rho_0} \boldsymbol{g}, \tag{2.1a}$$

$$\boldsymbol{\nabla}^* \cdot \boldsymbol{u}^* = 0. \tag{2.1b}$$

Here, $\boldsymbol{u}^*$ is the velocity field, ρ_0 is the reference density, ν is the kinematic viscosity, $\boldsymbol{g} = -g\hat{\boldsymbol{k}}$ is the gravitational acceleration, and ρ^* and Π^* represent the density and pressure deviations from the background density profile and the hydrostatic pressure balance, respectively. The total density ρ_{tot} is decomposed into

$$\rho_{tot}(\boldsymbol{x}^*, t^*) = \rho_0 + \rho_b^*(z^*) + \rho^*(\boldsymbol{x}^*, t^*), \tag{2.2}$$

where the background density ρ_b^* varies only with z^*. In the present study, ρ_b^* decreases linearly with z^*, which leads to a uniform buoyancy frequency $N = \sqrt{-(g/\rho_0)(\mathrm{d}\rho_b^*/\mathrm{d}z^*)}$. The evolution of ρ^* follows the advection–diffusion equation,

$$\frac{\partial \rho^*}{\partial t^*} + \boldsymbol{\nabla}^* \cdot (\rho^* \boldsymbol{u}^*) + w^* \frac{\mathrm{d}\rho_b^*}{\mathrm{d}z^*} = \kappa \, \nabla^2 \rho^*, \tag{2.3}$$

where κ is the diffusivity of density.

By non-dimensionalizing (2.1) and (2.3) using a characteristic length scale L, velocity scale U_0, and time scale L/U_0, and rescaling ρ^* and Π^* as

$$\rho^* \sim \frac{N^2 L}{g} \rho_0, \quad \Pi^* \sim \rho_0 U_0^2, \tag{2.4a,b}$$

respectively, we obtain the dimensionless governing equations

$$\frac{\partial \boldsymbol{u}}{\partial t} + \boldsymbol{u} \cdot \boldsymbol{\nabla} \boldsymbol{u} = -\boldsymbol{\nabla} \Pi + Re^{-1} \nabla^2 \boldsymbol{u} - Fr^{-2} \rho \hat{\boldsymbol{k}}, \tag{2.5a}$$

$$\boldsymbol{\nabla} \cdot \boldsymbol{u} = 0, \tag{2.5b}$$

$$\frac{\partial \rho}{\partial t} + \boldsymbol{u} \cdot \boldsymbol{\nabla} \rho - w = (Re\, Pr)^{-1} \nabla^2 \rho. \tag{2.5c}$$

Here, the Reynolds, Froude and Prandtl numbers are

$$Re = \frac{U_0 L}{\nu}, \quad Fr = \frac{U_0}{NL}, \quad Pr = \frac{\nu}{\kappa}, \tag{2.6a–c}$$

respectively. In this paper, U_0 is chosen such that dimensionless velocity in the base flow varies between $+1$ and -1, and L is chosen such that the scaled wavelength of the base flow in the horizontal directions is 2π. In the remainder of this paper, we set Re to 1600 and Pr to 0.70, and focus on the effects of Fr on the dynamics. The choice of Re helps to keep the computational demands of DNS (§ 3) manageable.

We consider the 2-D base flow given by

$$(U, V, W) = (\sin x \cos y, -\cos x \sin y, 0), \tag{2.7}$$

for $x, y \in [0, 2\pi)$ at $t = 0$, which consists of an array of columnar vortices as illustrated in figure 1. The base flow is periodic in both horizontal directions, x and y, and uniform in z. The pressure field P_0, streamfunction ψ, and vertical component of vorticity Ω_z associated with the base flow are

$$P_0 = \tfrac{1}{4}(\cos 2x + \cos 2y), \quad \psi = \sin x \sin y, \quad \Omega_z = 2 \sin x \sin y, \tag{2.8a–c}$$

respectively. The streamfunction and vorticity are related via $\nabla^2 \psi = -\Omega_z$. Incidentally, for this base flow, ψ and Ω_z have the same dependence on x and y. Due to viscous effects, the base flow velocities (U, V) and pressure (P_0) would decay as $\exp(-2t/Re)$ and

$\exp(-4t/Re)$, respectively (see e.g. Kim & Moin 1985), in the absence of flow instabilities. Our linear stability analysis detailed below, however, will focus on the base flow at $t = 0$, disregarding its considerably slow decay ($Re \gg 1$) due to viscosity.

We seek infinitesimal, three-dimensional (3-D) perturbations to the base flow that are expressed in normal modes in the z-direction:

$$(u', v', w', \rho', p') = (\hat{u}, \hat{v}, \hat{w}, \hat{\rho}, \hat{p}) \exp(\mathrm{i}kz + \sigma t) + \text{c.c.}, \tag{2.9}$$

where the $\hat{}$ quantities vary in (x, y). For simplicity, all primes on the perturbation variables will be dropped for the remainder of this paper. Linearizing the governing equations (2.5) for the base flow (2.7) yields the generalized eigenvalue problem

$$\sigma \begin{bmatrix} \boldsymbol{\Delta} & & \\ & \boldsymbol{\Delta} & \\ & & \boldsymbol{I} \end{bmatrix} \begin{bmatrix} \hat{u} \\ \hat{v} \\ \hat{\rho} \end{bmatrix} = \begin{bmatrix} \boldsymbol{L}_{uu} & \boldsymbol{L}_{uv} & \boldsymbol{L}_{u\rho} \\ \boldsymbol{L}_{vu} & \boldsymbol{L}_{vv} & \boldsymbol{L}_{v\rho} \\ \boldsymbol{L}_{\rho u} & \boldsymbol{L}_{\rho v} & \boldsymbol{L}_{\rho\rho} \end{bmatrix} \begin{bmatrix} \hat{u} \\ \hat{v} \\ \hat{\rho} \end{bmatrix}, \tag{2.10}$$

where $\boldsymbol{I}$ is an identity matrix, and the other linear operators are as follows:

$$\Delta = \partial_{xx} + \partial_{yy} - k^2, \tag{2.11a}$$

$$\boldsymbol{L}_{uu} = (-\Delta + \partial_{xx})(U\,\partial_x + V\,\partial_y + \partial_x U) + \partial_{xy}(\partial_x V) - \partial_x(U\,\partial_x + V\,\partial_y)\,\partial_x + Re^{-1}\,\Delta^2, \tag{2.11b}$$

$$\boldsymbol{L}_{uv} = (-\Delta + \partial_{xx})\,\partial_y U + \partial_{xy}(\partial_y V + U\,\partial_x + V\,\partial_y) - \partial_x(U\,\partial_x + V\,\partial_y)\,\partial_y, \tag{2.11c}$$

$$\boldsymbol{L}_{u\rho} = Fr^{-2}\,(\mathrm{i}k)\,\partial_x, \tag{2.11d}$$

$$\boldsymbol{L}_{vu} = (-\Delta + \partial_{yy})\,\partial_x V + \partial_{yx}(\partial_x U + U\,\partial_x + V\,\partial_y) - \partial_y(U\,\partial_x + V\,\partial_y)\,\partial_x, \tag{2.11e}$$

$$\boldsymbol{L}_{vv} = (-\Delta + \partial_{yy})(U\,\partial_x + V\,\partial_y + \partial_y V) + \partial_{xy}(\partial_y U) - \partial_y(U\,\partial_x + V\,\partial_y)\,\partial_y + Re^{-1}\,\Delta^2, \tag{2.11f}$$

$$\boldsymbol{L}_{v\rho} = Fr^{-2}\,(\mathrm{i}k)\,\partial_y, \tag{2.11g}$$

$$\boldsymbol{L}_{\rho u} = -(\mathrm{i}k)^{-1}\,\partial_x, \tag{2.11h}$$

$$\boldsymbol{L}_{\rho v} = -(\mathrm{i}k)^{-1}\,\partial_y, \tag{2.11i}$$

$$\boldsymbol{L}_{\rho\rho} = -(U\,\partial_x + V\,\partial_y) + (Re\,Pr)^{-1}\Delta. \tag{2.11j}$$

The full derivation of this linear system is given in Appendix A. A formulation similar to the present one to identify 3-D perturbations in a 2-D base flow (thus referred to as '2B3P') was used successfully to analyse experimental data from a stratified inclined duct (Chomaz 2018; Lefauve *et al.* 2018). The eigenvalue problem (2.10) is solved numerically using the MATLAB `eig` function. The differential operators along the periodic x- and y-directions are discretized with the Fourier differentiation matrix (Weideman & Reddy 2000), ensuring the horizontal periodicity of the resulting eigenmodes. The size of the eigenvalue problem is considerably large: using $\hat{N}$ Fourier points to discretize one horizontal direction results in two matrices of size $3\hat{N}^2$ by $3\hat{N}^2$ in (2.10). We used $\hat{N} = 64$ and 72 to solve the linear system, which produced nearly identical physical eigenvalues and eigenmodes between the two $\hat{N}$ values. Unphysical, spurious eigenmodes may arise, which are identifiable through a comparison of results from the two $\hat{N}$ values tested.

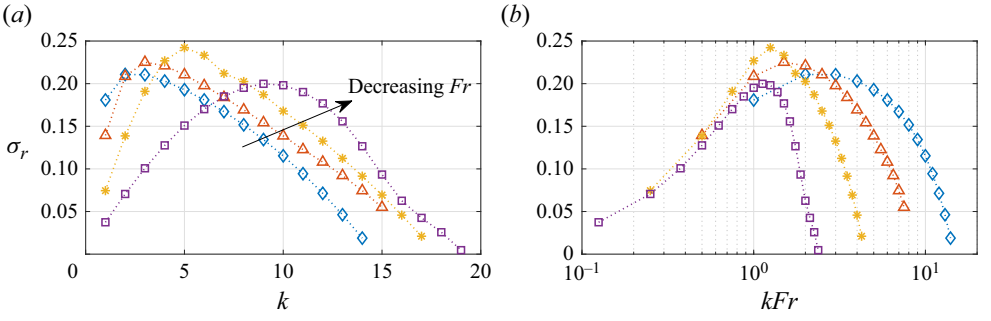

Figure 2. Growth rate σ_r plotted against (*a*) k and (*b*) $k\,Fr$ for the solution branch containing the fastest-growing mode: ◇, $Fr = 1.0$; △, $Fr = 0.5$; ∗, $Fr = 0.25$; □, $Fr = 0.125$.

2.2. *Linear dispersion relation*

Our investigation will focus on the effects of varying Fr, specifically for $Fr \in \{1, 1/2, 1/4, 1/8\}$. We selected this range of Fr because, as we will demonstrate, the fastest-growing modes at these values exhibit zigzag-like properties. Billant & Chomaz (2000*c*) observed zigzag instabilities in vortex dipoles when $Fr < 0.2$. The apparent inconsistency in the Fr ranges associated with zigzag instabilities arises from the difference in the choices of velocity and length scales used to define Fr. This distinction is also crucial for comparing dimensional quantities across different set-ups, as we discuss later in this subsection. We will report DNS conducted in a triply periodic domain for these Fr values in § 3. For linear stability analysis, we vary the vertical wavenumber k within the range 1–20 (integers only) due to the constraint that only integer modes of k are permissible in the DNS for domain height 2π. We display the solution branch that produces the fastest-growing mode across all wavenumbers for each Fr in figure 2. For this specific branch of eigenmodes, the imaginary part of σ is zero, i.e. $\sigma_i \equiv \mathrm{Im}(\sigma) = 0$, suggesting that all these modes are stationary. Another solution branch (not shown in figure 2) that emerges from the stability analysis corresponds to the pure hyperbolic (PH) mode that was investigated by Hattori *et al.* (2021). The PH modes can be easily distinguished from the solution branch shown in figure 2 as the PH modes have a non-zero frequency ($\sigma_i \neq 0$). The instability mechanism of the PH mode does not require stratification (Leblanc & Godeferd 1999), and the most unstable mode occurs at $k = 0$, i.e. when the perturbation structure is 2-D.

Figure 2 demonstrates that the growth rate $\sigma_r \equiv \mathrm{Re}(\sigma)$ initially increases with k for smaller values of k, and subsequently decreases as k increases further. The fastest-growing k (table 1) shifts to the left as Fr increases. When k is adjusted by multiplying it by Fr, the increasing flank of the curves nearly collapses, and the peak growth rate occurs within a narrow range of $k\,Fr$ between 1.1 and 2.0, i.e. for the most unstable mode,

$$k \sim Fr^{-1}. \tag{2.12}$$

Or, in dimensional form, the fastest-growing wavelength $\lambda_z^* \equiv (2\pi/k)L$ scales as

$$\lambda_z^* \sim (2\pi)(U_0/N). \tag{2.13}$$

The maximum non-dimensional growth rates σ, summarized in table 1, exhibit no significant variability with respect to Fr. Accordingly, the dimensional growth rate

Fr	k	σ
1.000	2	$0.2108 + 0.0000\mathrm{i}$
0.500	3	$0.2251 + 0.0000\mathrm{i}$
0.250	5	$0.2422 + 0.0000\mathrm{i}$
0.125	9	$0.1998 + 0.0000\mathrm{i}$

Table 1. The most unstable mode at each Fr considered.

$\sigma^* \equiv \sigma U_0/L$ scales as

$$\sigma^* \sim U_0/L. \tag{2.14}$$

In their examination of zigzag instability, Billant & Chomaz (2000*b*) (hereafter referred to as BC00) observed that the vertical scale most susceptible to zigzag instability in a vortex pair scales with U_0/N, i.e. (2.13), and the maximum growth rate with U_0/L, i.e. (2.14). These scalings are markedly similar to the results presented above for the vortex array. The scaling (2.12) is in contrast to the elliptic instability for which the fastest-growing wavenumber and growth rate both increase with Fr (see e.g. figure 2 of Billant & Chomaz 2000*c*). Figure 2 presents dispersion relations that are at least qualitatively similar to those identified by BC00 (see e.g. their figure 7), i.e. the growth rate σ_r peaks at a non-zero vertical wavenumber k. This contrasts with horizontally sheared flows, which feature a one-dimensional velocity profile varying along the horizontal direction with gravity oriented in the spanwise direction (Deloncle, Chomaz & Billant 2007; Arobone & Sarkar 2012; Lucas, Caulfield & Kerswell 2017). In such flows, the most unstable modes have a zero vertical wavenumber, an observation considered by Deloncle *et al.* (2007) as an extension of Squire's theorem to stratified flows.

Additionally, the primary instability of a TG vortex array resembles the zigzag instability observed in vortex dipoles in several key aspects. For both cases, the eigenvalues for the fastest-growing modes are real ($\sigma_i = 0$), and the dispersion relation reveals an approximately linear relationship between the dimensionless growth rate (σ_r) and small values of $k\,Fr$, as shown in figure 9 of Billant & Chomaz (2000*c*). Data for the vortex array included in figure 2(*b*) suggest a linear relation (not shown) between σ_r and $k\,Fr$, which collapses data across various Fr values between 0.125 and 0.5 for $k\,Fr \lesssim 1$. Furthermore, the magnitude of the peak growth rates, when dimensionalized, lies between 0.20 and 0.24 times U_0/L, or 0.63–0.75 times U_0/D, where $D = \pi L$ represents the distance between the centres of two adjacent oppositely signed vortices (figure 1). Using similar metrics, the dimensional growth rate σ^* typically ranges from 0.6 to 0.7 times U_0/D in the dipole scenario, according to figure 9 of Billant & Chomaz (2000*c*), where $D \approx L$ following figure 1 of BC00.

As discussed earlier, our study focuses on the range $0.125 \leq Fr \leq 1$, where the primary instability exhibits many characteristics similar to the zigzag instability. For Fr values outside this range, the PH mode (Hattori *et al.* 2021) shows a higher growth rate across all wavenumbers. Specifically, for $Fr < 0.125$, the dispersion relation of the zigzag modes at $Fr = 0.0625$ (not shown) exhibits a reduced maximum growth rate, and the latter is also lower than that of the PH mode at this Fr. For larger Fr values, figure 8 of Hattori *et al.* (2021) indicates that the PH mode becomes the dominant instability for $Fr > \pi$, surpassing the zigzag modes. Currently, we do not have sufficient data to pinpoint the exact transition point in terms of Fr between zigzag and PH modes, and this critical Fr value might also vary with Re. Nonetheless, the evidence available seems to suggest that this

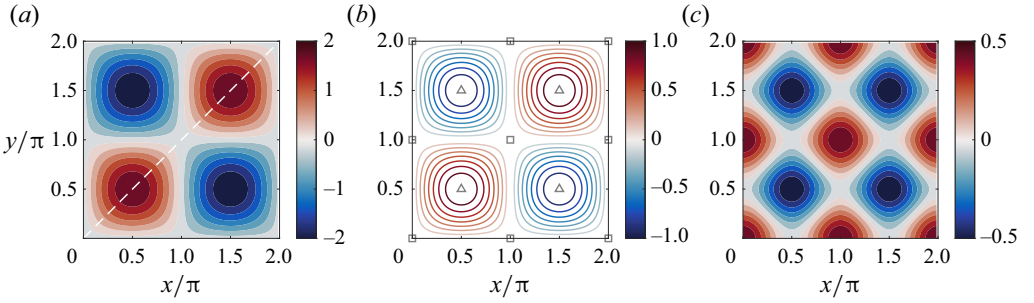

Figure 3. Base flow characteristics: (*a*) vorticity Ω_z, (*b*) streamfunction ψ, and (*c*) pressure P_0. The dashed line in (*a*) marks the line $y = x$, along which a vertical transect is illustrated in figure 5. The contours of ψ are shown in (*b*) for $0.125 \leq |\psi| \leq 0.875$, with an interval of 0.125 between adjacent contour levels. The symbol Δ in (*b*) indicates the location of an elliptical stagnation point, and $\square$ indicates a hyperbolic stagnation point.

transitional Fr is likely to be greater than 1 and probably of $O(1)$. In summary, within the Fr range $O(0.1)$ to $O(1)$, the zigzag mode, whose most unstable eigenmode appears to be 3-D ($k \neq 0$), tends to dominate. Outside this Fr range, the fastest-growing instability shifts to the 2-D PH modes ($k = 0$), whose instability mechanism does not rely on stratification.

2.3. *Instability mechanism*

We now turn our attention to the most unstable eigenmode at $k = 3$ for $Fr = 0.5$, using it as an example to shed light on the underlying instability mechanism. The characteristics of the 2-D base flow are illustrated in figure 3, while the horizontal structure of the 3-D eigenmode is displayed in figure 4. In particular, figure 4(*a*), which shows the vertical vorticity perturbation $\omega_z \equiv \partial_x v - \partial_y u$, reveals horizontal structures similar to those presented in figure 5 of Hattori *et al.* (2021) (hereafter referred to as H21). These structures are identified by H21 as MH modes. In line with our results in § 2.2, H21 demonstrated that the MH modes, specifically the branch with $\sigma_i = 0$, yield the highest growth rate σ_r for their cases with $Fr \leq \pi/2$ (equivalently, $F_h \leq 0.5$ in the H21 terminology, with $F_h \equiv Fr/\pi$ due to the differences in the definitions). Furthermore, H21 noted an increase in the fastest-growing k as Fr decreased from 0.2π to 0.1π, consistent with the expected behaviour for zigzag instabilities.

H21 classified these MH modes as a subtype of hyperbolic instabilities, alongside PH modes, which are independent of stratification, and SH modes, which result from the phase shifts in internal gravity waves induced by PH modes. The 'mixed' nature of these modes arises, according to H21, from the vorticity distribution being a combination of both PH and SH instabilities. H21 did not describe the physical mechanism of MH modes in detail. Here, we will take a different perspective and elucidate how the MH modes become unstable by drawing parallels to the zigzag instabilities in the vortex dipole case studied by BC00.

To start, it is useful to summarize the zigzag instability mechanism for dipoles as outlined by BC00. The mechanism begins with an initial pressure distribution P_0 associated with the base flow. A height-varying horizontal displacement of the dipole column induces a vertical pressure gradient, leading to isopycnal deformation (as shown in their figure 3*a*) due to the hydrostatic balance between the density perturbation ρ and pressure perturbation p. This mechanism, which was also considered by Basak & Sarkar (2006), is described by the linearized vertical momentum equation (A1*c*) in hydrostatic

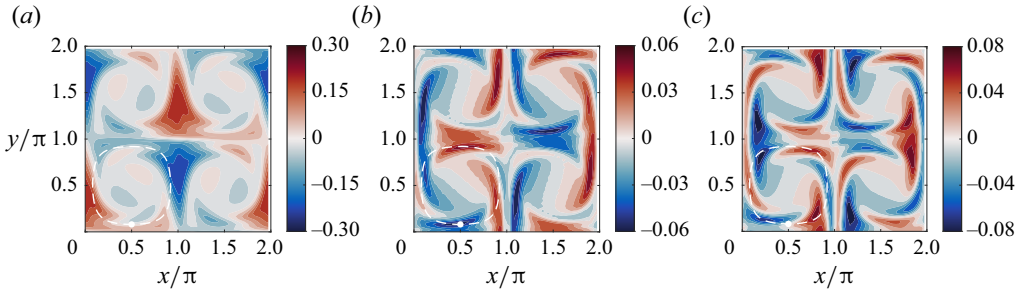

Figure 4. Horizontal transect of perturbation (*a*) ω_z at $z = z_0$, (*b*) ρ at $z = z_+$, and (*c*) w at $z = z_+$, for the eigenmode with $k = 3$ at $Fr = 0.5$. The heights z_0 and z_+ are specified in figure 5. The amplitude of the eigenmode is normalized such that the kinetic energy associated with the horizontal perturbation velocities (u, v) constitutes 1 % of the kinetic energy in the base flow (U, V). The dashed line indicates the streamline corresponding to $\psi = 0.25$, and the solid dot indicates the starting point of a particle trajectory considered in figure 6.

balance, i.e.

$$-\partial_z p \approx Fr^{-2}\,\rho. \tag{2.15}$$

The displacement of isopycnals due to ρ initiates a vertical velocity w as per the linearized density equation (A6), assuming negligible diffusion,

$$\partial_t \rho + (U\,\partial_x + V\,\partial_y)\rho \approx w, \tag{2.16}$$

where the right-hand side arises due to the perturbation vertical velocity w, and the non-dimensional background density gradient $\mathrm{d}\rho_b/\mathrm{d}z = -1$. The linear equation (A6) indicates that a fluid parcel, while being transported by the base flow (U, V), undergoes density fluctuations directly coupled to vertical velocity w. A distinct feature of the zigzag instability is its stationarity, i.e. $\sigma_i = 0$, as discussed in § 2.2. As a result, the motion of a fluid parcel undergoing zigzag instability can be seen as traversing a loop that samples a stationary, horizontal pattern of the flow (see figure 3(*a*) of BC00), rather than linear oscillation around an equilibrium position as in an internal wave ($\sigma_i \neq 0$). This vertical motion induced by this mechanism causes straining in the vertical direction, i.e. $\partial_z w \neq 0$, leading to diverging horizontal perturbation velocities ($\partial_x u + \partial_y v \neq 0$). The horizontal perturbation velocities (u, v) further displace the dipole horizontally and introduce rotational 'twists' within the dipole, thus amplifying the initial perturbations and completing the feedback loop that characterizes the zigzag instability mechanism.

Some key features of the TG base flow are revisited in figure 3 in light of the zigzag mechanism. The TG base flow vorticity Ω_z (figure 3*a*) and streamfunction ψ (figure 3*b*) have the same structure over the x–y plane, which means that a fluid parcel advected by the base flow would encounter a constant Ω_z along a streamline. Two types of stagnation points exist (figure 3*b*): elliptical and hyperbolic. Figure 3(*c*) demonstrates that the base flow pressure P_0 attains its highest values at the hyperbolic stagnation points, and lowest at the elliptical stagnation points.

To leading order, the perturbations to the vortex dipole analysed by BC00 involve a simple horizontal translation of the vortical structure, resulting in a sinusoidal deformation of the vortex column, as illustrated in their figure 3. In the TG case, the ω_z perturbations displayed in figure 4(*a*) reveal more complex spatial variations than would be expected from a mere horizontal translation of columnar vortices. The vertical–horizontal transects presented in figure 5 demonstrate how the base flow Ω_z in figure 5(*a*) is modified by the

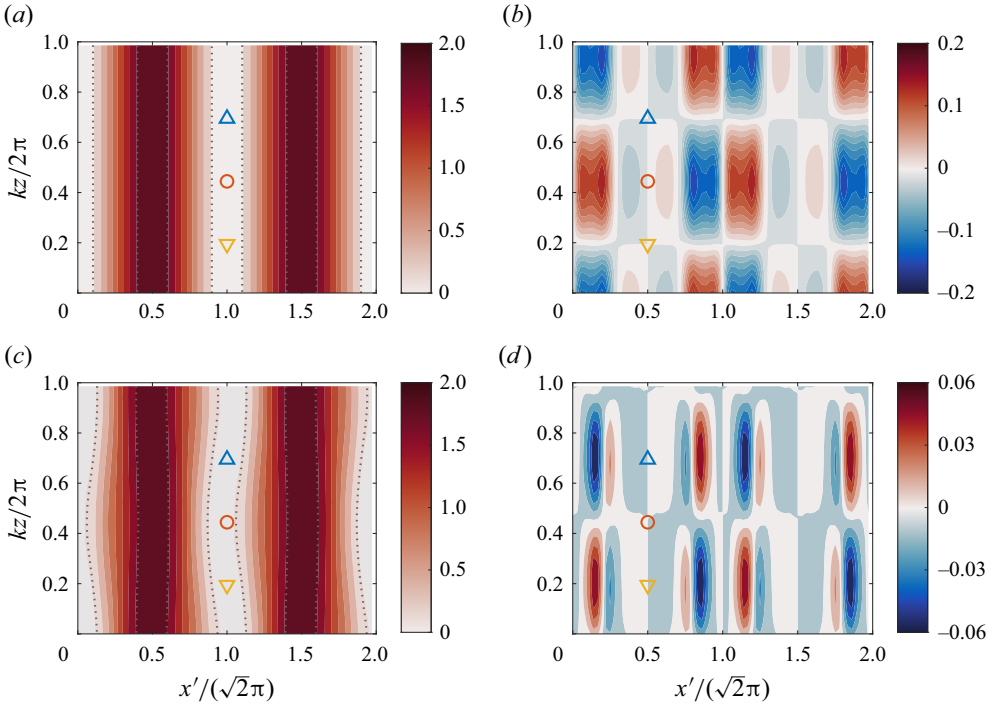

Figure 5. Vertical–horizontal transect of (*a*) base flow Ω_z, (*b*) perturbation ω_z, (*c*) $\Omega_z + \omega_z$, and (*d*) vertical velocity w. The horizontal axis x' represents the distance from the origin along the line $y = x$, indicated by a white dashed line in figure 3. One full vertical wavelength is shown in z. Dotted lines in (*a*) and (*c*) display vertical vorticity contours at 0.2 and 1.8, respectively. Symbols Δ and ∇ mark the heights z_+ and z_-, respectively, where w attains its maximum magnitude, and $\circ$ is the height $z_0 = (z_+ + z_-)/2$, where ω_z reaches the maximum magnitude.

perturbation ω_z in figure 5(*b*) to form the 'bent' pattern in figure 5(*c*), similar to the dipole scenario. Figure 5(*b*) suggests that large magnitudes of ω_z are located at the 'edges' of the vortex column, leading to pronounced bending at these locations – for instance, see the contour of the perturbed vorticity $\Omega_z + \omega_z$, at 0.2 in figure 5(*c*). Conversely, the magnitude of ω_z near the centre of the columns is relatively small, resulting in less pronounced bending and in a direction opposite to that at the edges, as shown by the $\Omega_z + \omega_z$ contour at 1.8 in figure 5(*c*). Strictly speaking, the zigzag instability involves only a displacement of the vortex core as a whole. The vortex structure depicted here also shows an internal deformation of the vortex, which might seem closer to the elliptic instability in appearance (see e.g. figure 4 of Otheguy *et al.* 2006). However, it will be demonstrated in the following that the instability mechanism is indeed 'zigzag-like'.

Following the BC00 argument, the deformation of the vortex columns (figure 5*c*) produces a horizontal shift of the associated pressure field P_0 (figure 3*c*). This shift results in a z-dependent pressure field ($\partial_z p \neq 0$), which is associated with density perturbations ρ (figure 4*b*) through the hydrostatic balance (2.15). The ρ perturbation is then associated with vertical velocities w (figure 4*c*) via (2.16). The vertical structures of such w perturbations are presented in figure 5(*d*). Consistent with figure 3(*b*) of BC00, figure 5(*d*) demonstrates that w vanishes at $z = z_0$ where $|\omega_z|$ reaches maximum, i.e. where the vortex column experiences the greatest horizontal displacement. The magnitude of w peaks a

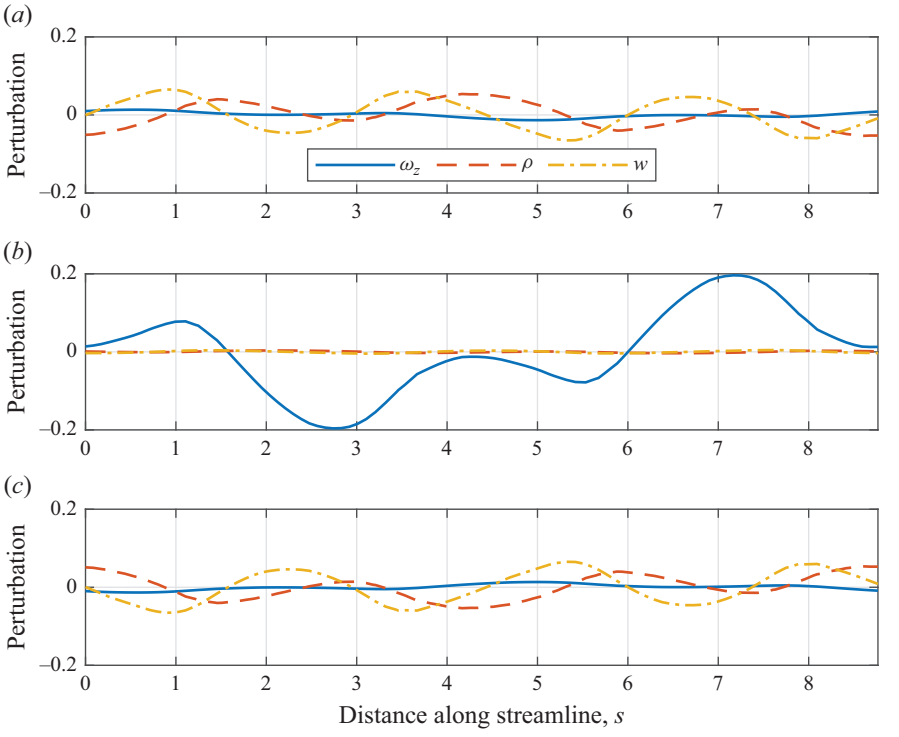

Figure 6. Profiles of perturbation ω_z, ρ and w along a specific base flow streamline ($\psi = 0.25$) at various heights: (*a*) $z = z_+$, (*b*) $z = z_0$ and (*c*) $z = z_-$. This particular streamline is marked in figure 4 with a white dashed line. The profiles commence at the location indicated by a solid dot in figure 4, and trace the ψ contour in the anticlockwise direction, following the path of a fluid parcel moving according to the base flow (U, V).

quarter vertical wavelength away from z_0 at z_+ or z_-, coinciding with the heights at which $|\omega_z|$ is at its lowest.

The connection between the ρ and w perturbations, shown in figures 4(*b*) and 4(*c*), respectively, becomes clear when considering (2.16) within the scenario of a fluid parcel moving with the base flow. We focus on a particular streamline, marked by a dashed line in figure 4, and examine perturbations along this streamline at various heights as shown in figure 6. In terms of the ω_z perturbation, as discussed previously, its magnitude reaches the maximum at $z = z_0$, and nearly vanishes at $z = z_+$ and z_-. In contrast, the perturbations ρ and w exhibit significant magnitudes at $z = z_+$ and z_-, where both quantities are of the same magnitude but oppositely signed at $z = z_+$ and z_-, respectively, for any given point along the streamline, reflecting the anti-symmetry about the height $z = z_0$. The rate of change of ρ with respect to the distance (s) along the streamline, $\partial_s \rho$, a proxy for the left-hand side of (2.16), is closely associated with w, as evidenced by figure 6. For example, $\partial_s \rho > 0$ tends to coincide with $w > 0$, and vice versa. This confirms that ρ and w are coupled via (2.16) at a given height of the columnar vortex, highlighting a key element in the zigzag mechanism.

With isopycnal deformations inducing z-dependent w perturbations, $\partial_z w$ becomes non-zero, balanced by non-zero $\partial_x u + \partial_y v$ in the continuity equation. Figure 7(*a*) shows the flow pattern over an x–y plane, where the (u, v) velocities typically originate from regions of vertical convergence ($\partial_z w < 0$) and move towards regions of divergence ($\partial_z w > 0$) to maintain continuity. This complex flow pattern results in the formation of vortical

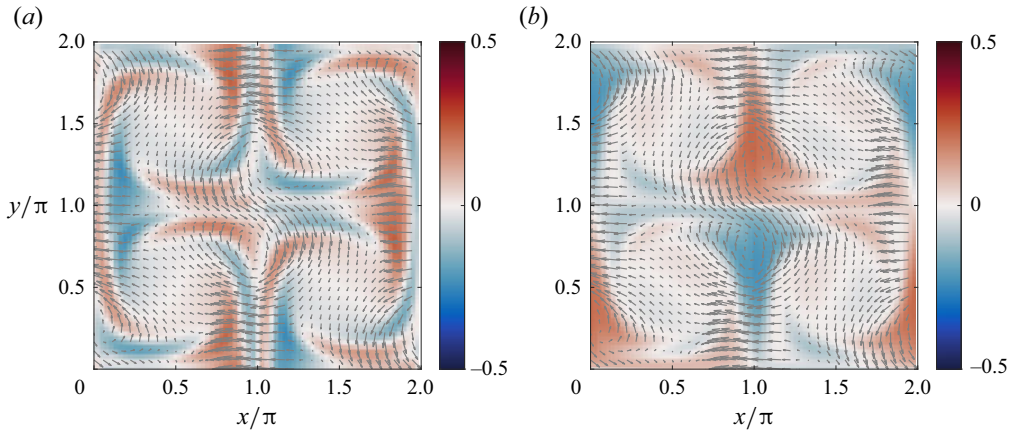

Figure 7. Horizontal velocity vector field (u, v) visualized by arrows, overlaid by colour maps showing (a) ω_z, and (b) $\partial_z w$, at $z = z_0$.

structures (figure 7*b*), including a pair of vortices with opposite signs near the hyperbolic stagnation point at $(x, y) = (\pi, \pi)$. Such vortical perturbations, manifested as ω_z, complete the dynamical feedback loop initiated by the deformation of the columnar vortices (figure 4*a*). As a result, the instability is expected to grow, following the dynamics outlined above, which closely resemble those of the zigzag instability proposed by BC00.

3. Direct numerical simulations

3.1. *Numerical configuration*

To examine the nonlinear evolution of the unstable modes identified in § 2 and their role in the breakdown of columnar TG vortices into turbulence, we conducted DNS using the lattice Boltzmann (LB) method. The LB flow solver, known as 'OpenLB', was developed by Krause *et al.* (2020) and has been adapted to solve the Boussinesq-approximated Navier–Stokes equations (2.5) by Guo, Zhou & Wong (2023) for wall-bounded stratified turbulent flows. An overview of the LB solver is provided in Appendix B. Additionally, we performed further validation of this LB solver against pseudo-spectral DNS in a triply periodic configuration, an effort that is also documented in Appendix B.

We carried out four simulations of the columnar TG flow within a triply periodic domain of length 2π in each direction, employing the same parameters examined in § 2. The specifics of these simulations are detailed in table 2. The computational mesh is uniform and isotropic. The grid spacing is no more than twice the Kolmogorov scale during peak dissipation. The simulations were initiated with the base flow defined by (2.7) at $t = 0$, with the phases of the sinusoidal functions slightly altered by random noise. Specifically, the initial conditions were set as

$$(U, V, W) = [\sin(x + \epsilon_1)\cos(y + \epsilon_2), -\cos(x + \epsilon_3)\sin(y + \epsilon_4), 0 + \sin(\epsilon_5)], \quad (3.1)$$

where the phase shifts (ϵ) are computer-generated pseudo-random numbers uniformly distributed within the range $[-0.01, 0.01]$. This introduction of low-level noise is critical for symmetry breaking and triggering instabilities, as suggested by Riley & de Bruyn Kops (2003) in their study of the turbulence generated by the breakdown of 3-D TG vortices.

Fr	(N_x, N_y, N_z)	Δt	$\bar{\sigma}$	k_{fgm}	λ_{fgm}	ℓ_v	Fr_v
1.000	(252, 252, 252)	1.44×10^{-4}	0.189	2	3.14	2.42	0.413
0.500	(252, 252, 252)	1.44×10^{-4}	0.198	3	2.09	1.84	0.272
0.250	(503, 503, 503)	7.22×10^{-5}	0.191	5	1.26	1.09	0.229
0.125	(503, 503, 503)	3.61×10^{-5}	0.158	9	0.70	0.74	0.169

Table 2. Parameters of DNS for $(Re, Pr) = (1600, 0.7)$ and various Froude numbers. Here, (N_x, N_y, N_z) are the number of lattice points used in each direction, Δt is the time step size, $\bar{\sigma}$ is the estimated overall linear growth rate (§ 3.3), k_{fgm} and λ_{fgm} are the observed fastest-growing wavenumber and wavelength, respectively, and ℓ_v and Fr_v are the vertical length scale (3.4) and Froude number (3.5), respectively, for the time when the perturbation kinetic energy E_k in (3.3*a*,*b*) first exceeds 0.01.

3.2. *Flow phenomenology*

The evolution of the flow is visualized through volume-rendered colour images of vertical vorticity in figure 8 for the case $Fr = 0.5$. The sequence starts with an image at $t = 32$, where the vortex structure is similar to the base flow (figure 1), with weak perturbations manifesting as corrugations on the surface of the vortex tube. By $t = 40$ (top right image), these corrugations have intensified. Images in the middle row reveal the emergence of nonlinear dynamics, such as secondary perturbations between and then within the columns, which quickly evolve into turbulence for $44 \leq t \leq 52$. The bottom row illustrates the decay of turbulence from its maximum intensity. Figure 9 shows the corresponding sequence of images for $Fr = 0.25$. Relative to the $Fr = 0.5$ case, the corrugations on the vortex tube surface appear at a finer vertical length scale, and the transition to a fully disorganized state at $t = 56$ (bottom left image) appears to occur more gradually as compared to the $Fr = 0.5$ case.

3.3. *The energetics*

The flow field can be decomposed into a vertically averaged component $\bar{\boldsymbol{U}} = (\bar{U}, \bar{V}, 0)$ and the fluctuation $\boldsymbol{u} = (u, v, w)$. The kinetic energy contained in the mean velocities can be quantified by

$$\bar{E}_k = \tfrac{1}{2}\langle \bar{\boldsymbol{U}} \cdot \bar{\boldsymbol{U}} \rangle, \tag{3.2}$$

where $\langle\cdot\rangle \equiv (2\pi)^{-3} \iiint (\cdot)\, \mathrm{d}x\, \mathrm{d}y\, \mathrm{d}z$ denotes volume average over the entire domain. There is no mean potential energy associated with the density perturbation ρ. Note that $\bar{\boldsymbol{U}}$ in general differs from the base flow (2.7) due to viscous decay and flow instabilities. The kinetic energy and potential energy contained in the fluctuation field are

$$E_k = \frac{1}{2}\langle \boldsymbol{u} \cdot \boldsymbol{u} \rangle, \quad E_p = \frac{1}{2\,Fr^2}\,\langle \rho^2 \rangle, \tag{3.3a,b}$$

respectively.

We examine the energetics in the system through figure 10, taking the $Fr = 0.5$ and 0.25 cases as an example. Figures 10(*a*,*b*) display energy on a linear scale, revealing that for a significant duration, up to $t \lesssim 40$ for $Fr = 0.5$, and $t \lesssim 45$ for $Fr = 0.25$, the kinetic energy is dominated by the vertically uniform (mean) component, $\bar{E}_k$. The mean kinetic energy slowly decays linearly due to viscosity at the anticipated rate $\exp(-4t/Re)$. Figures 10(*c*,*d*), where energy is plotted on a logarithmic scale, indicate that following the initial adjustments to the random noise, the fluctuation kinetic and potential energy

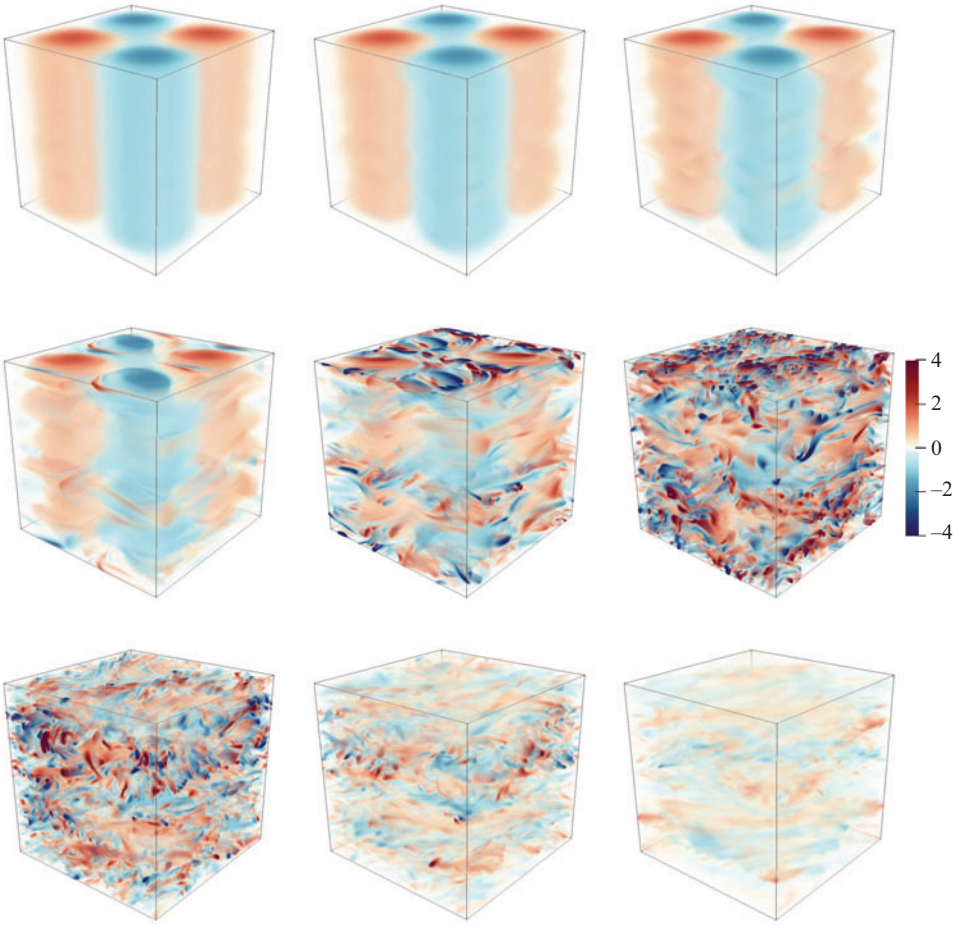

Figure 8. Snapshots of the vertical vorticity field from the DNS with $Fr = 0.5$. The initial image in the sequence was captured at time $t = 32$. Subsequent images are spaced at regular intervals of 4.0 units of time, arranged from left to right and top to bottom.

(E_k and E_p, respectively) grow linearly with time, i.e. $E_k, E_p \propto \exp(2\bar{\sigma}t)$. The overall growth rates $\bar{\sigma}$, which do not vary significantly across all four Fr cases, are tabulated in table 2. At $t \approx 40$ for $Fr = 0.5$ and $t \approx 45$ for $Fr = 0.25$, both E_k and E_p experience a significant upsurge as shown in the linear plots, alongside a rapid decline in the mean $\bar{E}_k$ as the flow transitions to turbulence. The fluctuation energies E_k and E_p depart from the linear trend and saturate by $t \approx 50$ for $Fr = 0.5$, and by $t \approx 55$ for $Fr = 0.25$, at which stage the mean energy component has been reduced significantly. Beyond this point, the fluctuating E_k becomes the dominant form of kinetic energy and starts to decrease rapidly, along with the potential energy E_p.

The growth in the fluctuation energy is contributed by various vertical wavenumbers k. In figure 11, we examine the vertical spectra of kinetic energy of E_k, denoted as $\tilde{E}_k$, as they vary with k and over time for $Fr = 0.5$. Figure 11(a) demonstrates the overall growth of kinetic energy across a range of vertical wavenumbers for $16 \leq t \leq 40$, coinciding with the linear growth phase of the instabilities (see figure 10c). The linear growth is non-uniform across wavenumbers. By $t = 24$, the mode of $k = 3$ has surpassed all other modes in terms

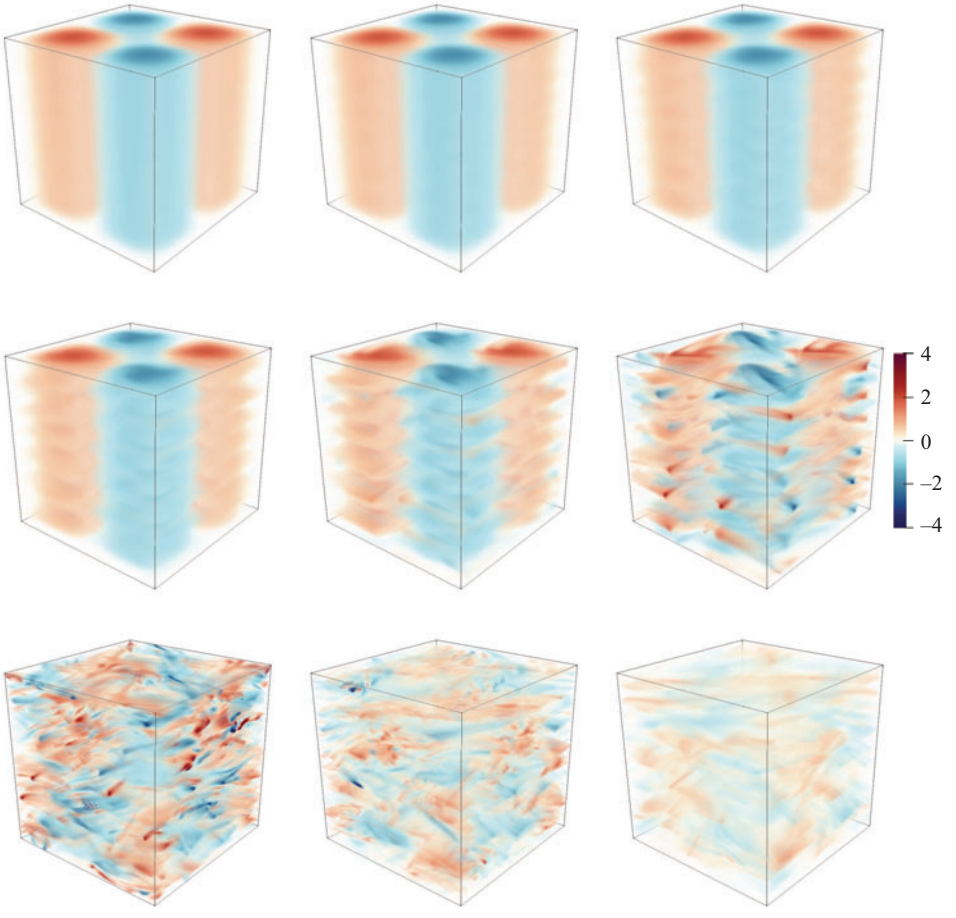

Figure 9. Same layout as figure 8 for the case with $Fr = 0.25$.

of the energy level. Incidentally, $k = 3$ is also the fastest-growing mode predicted by the linear stability analysis (table 1); more discussion on this will follow in the next subsection. Figure 11(b) shows that each mode of different k also follows its own rate of linear growth, $\sigma(k)$. Again, the mode with $k = 3$ gains the most energy during the linear growth stage of the instabilities.

In figure 12, we investigate the vertical length scale ℓ_v, which characterizes the energy-containing scales in the initially uniform z-direction. Similar to Zhou & Diamessis (2019), who used ℓ_v to characterize the vertical scale associated with spontaneously formed shear layers in stratified turbulent wakes, we define

$$\ell_v(t) \equiv 2\pi \int_{k_{min}}^{k_{nyq}} k^{-1}\, \tilde{E}_k(k, t)\, \mathrm{d}k \Big/ \int_{k_{min}}^{k_{nyq}} \tilde{E}_k(k, t)\, \mathrm{d}k, \tag{3.4}$$

where $k_{min} = 1.0$ is the minimum wavenumber, and k_{nyq} is the Nyquist wavenumber (k_{nyq} is 126 for $Fr \geq 0.5$, and 251 for $Fr < 0.5$). Figure 12 indicates that ℓ_v stays relatively constant over time after the initial transients, but exhibits a strong dependence on Fr. As Fr decreases, the vertical length scale that emerges before the breakdown of columnar vortices also decreases, again reminiscent of the anticipated scaling of zigzag instabilities.

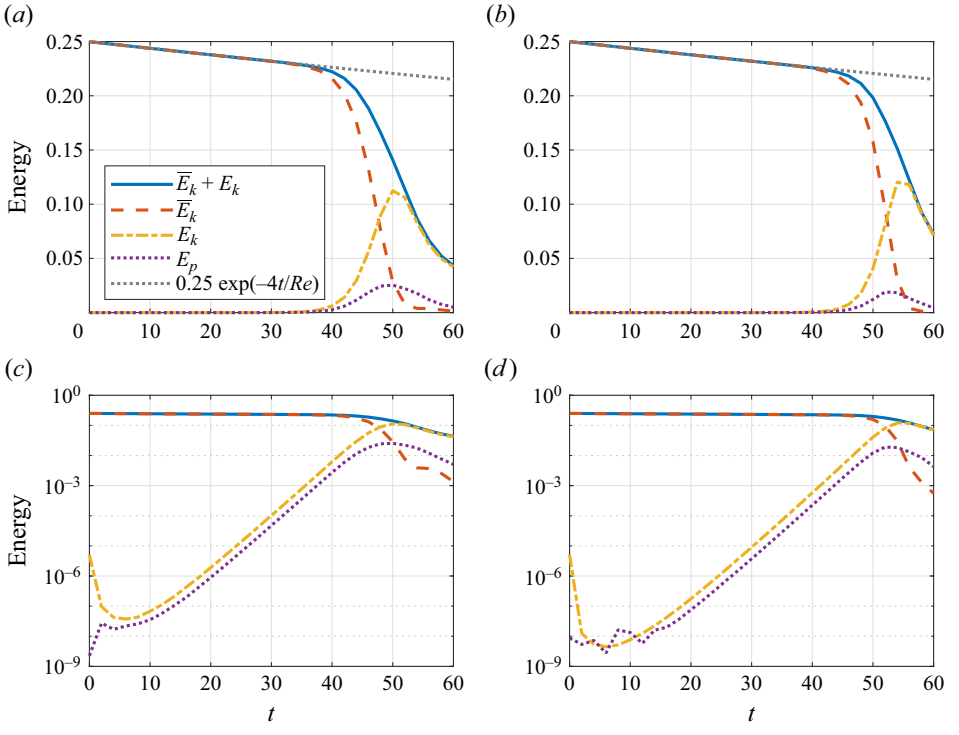

Figure 10. Time series of various energy components, for (*a*,*c*) $Fr = 0.5$ and (*b*,*d*) $Fr = 0.25$. Energy is plotted (*a*,*b*) on a linear scale, and (*c*,*d*) on a logarithmic scale.

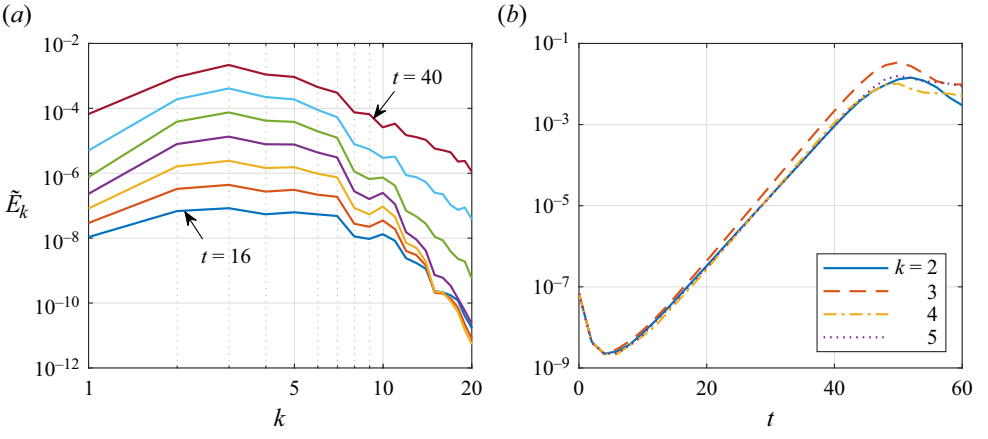

Figure 11. Sample fluctuation kinetic energy spectra for $Fr = 0.5$ displayed (*a*) as a function of k, and (*b*) as a function of t. For (*a*), the spectra are selected from $16 \leq t \leq 40$, at intervals of 4.0 time units, with the curves shifting upwards as time progresses.

To examine whether the dimensional vertical length scale $\ell_v^* \equiv \ell_v L$ follows the expected U_0/N scaling, it is helpful to examine an inverse vertical Froude number,

$$Fr_v^{-1} = \frac{\ell_v^* N}{U_0} = \frac{\ell_v}{Fr}. \tag{3.5}$$

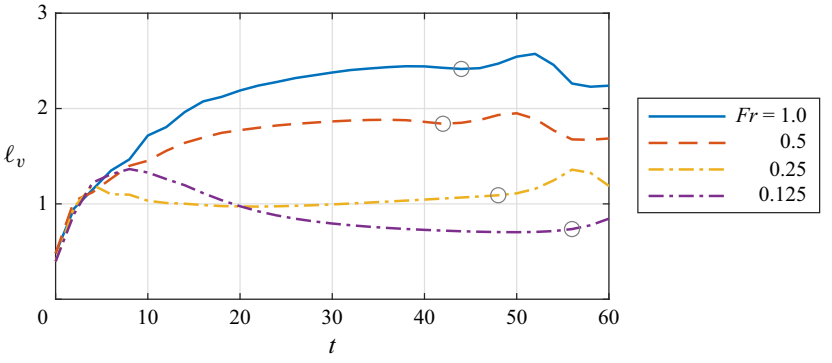

Figure 12. Time series of the energy-containing vertical length scale ℓ_v in (3.4), for different values of Fr. Grey circles indicate the time at which E_k first exceeds 0.01; the ℓ_v values at these times are tabulated in table 2 for comparison with λ_{fgm}.

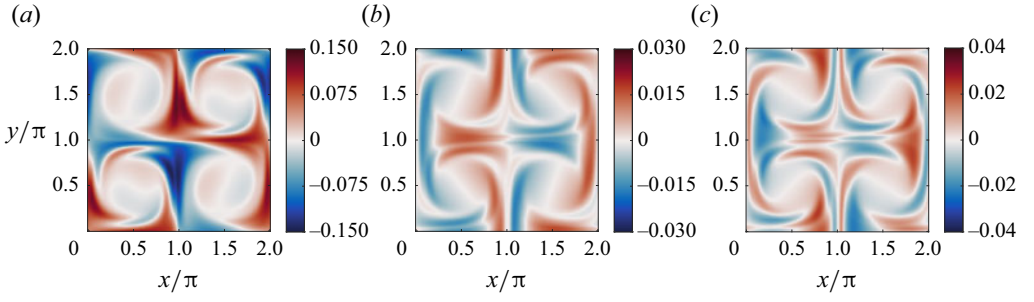

Figure 13. Flow structure observed at $t = 32$ in the DNS for $Fr = 0.5$. The layout is the same as figure 4. (*a*) The vertical vorticity perturbation ω_z displayed for $z = z_0$ where ω_z reaches its largest magnitude. (*b*,*c*) The ρ and w perturbations at $z_+ = z_0 + \lambda_{fgm}/4$.

Characteristic values of Fr_v are tabulated in table 2, where they exhibit the same order of magnitude and a decreasing trend as Fr decreases. This relationship between Fr_v and Fr is consistent with the results from forced DNS by Waite & Bartello (2004) and Brethouwer *et al.* (2007). In contrast, in the decaying turbulence simulations by Maffioli & Davidson (2016), Fr_v was observed to approach a relatively narrow range as the flow transitions towards relaminarization.

3.4. *Comparison with linear stability analysis*

In figures 13 and 14, we examine the flow structure in the DNS of $Fr = 0.5$, captured at $t = 32$ during the linear growth stage of the instabilities (figure 10). Figure 13 displays the perturbation field over the x–y plane. The ω_z field is taken at the height (z_0) where the ω_z magnitude is found to be at maximum, and ρ and w are shown at the height one-quarter vertical wavelength $\lambda_{fgm} \equiv 2\pi/k_{fgm}$ above z_0. Here, k_{fgm} is taken to be 3 following the observation in figure 11, which is also consistent with the linear stability analysis (figure 2). The pattern found in figure 13 is in strong agreement with the most unstable eigenmode presented in figure 4. Figure 14 displays a full vertical wavelength λ_{fgm} of the DNS field, exhibiting similarities to figure 4 where the fastest-growing eigenmode is presented. The DNS field presents additional complexities, likely due to the presence of multiple wavenumbers beyond the single wavenumber ($k = 3$) included in figure 5. The agreement

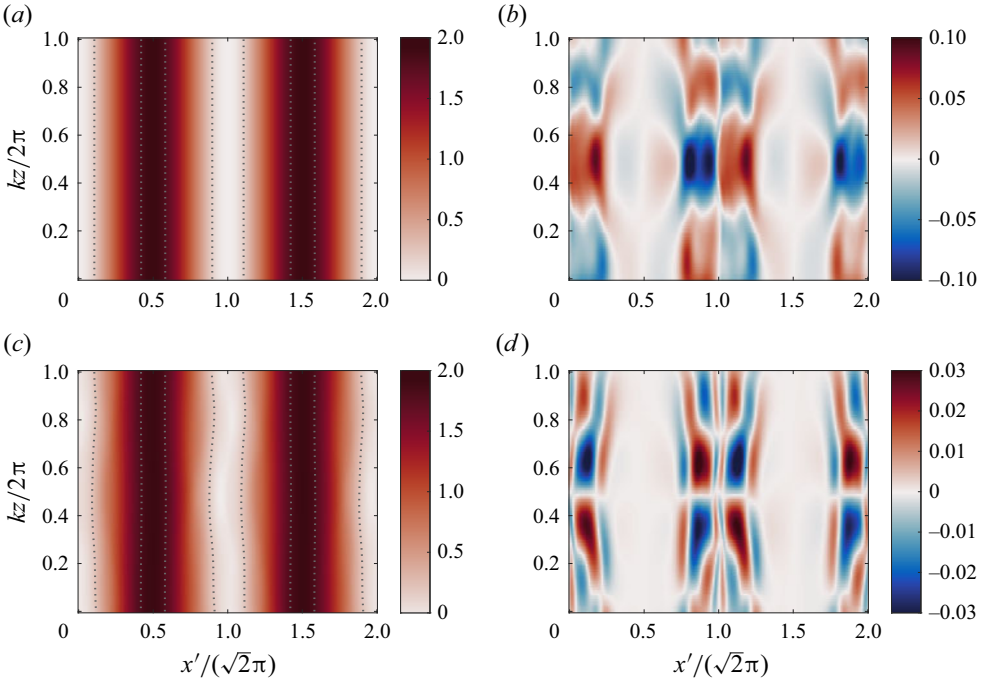

Figure 14. Vertical–horizontal transects of the DNS flow field at $t = 32$ for $Fr = 0.5$, presented in a layout identical to figure 5. One full wavelength according to the fastest-growing $k_{fgm} = 3$ is shown in the vertical. The vertically uniform component of vorticity, $\bar{\Omega}_z$, is calculated based on the vertically averaged flow field $\bar{U}$. Plots are for (*a*) $\bar{\Omega}_z$, (*b*) ω_z, (*c*) $\bar{\Omega}_z + \omega_z$, and (*d*) w.

in terms of flow structure between the DNS and linear stability analysis indicates that these linear modes are indeed vital in leading to the breakdown of the columnar vortices.

Figure 15 compares the predicted growth rates for each mode, shown previously in figure 2, with their DNS counterparts estimated from the time series of modal energy such as those shown in figure 11(*b*). The DNS growth rates are estimated over approximately 20 time units during which linear growth is observed; this period is determined through visual inspection of plots such as those in figure 11(*b*). The error bars associated with the σ estimates (not shown) are smaller than or similar in size to the symbols used in figure 15. The agreement between DNS and linear stability analysis is generally good, particularly in that the fastest-growing mode observed in the DNS has a vertical wavenumber matching the most unstable mode found using the linear stability analysis. This agreement underscores the pivotal role of linear instabilities in determining the structure of turbulence. The wavelength of the most unstable mode, λ_{fgm}, closely matches the energy-containing vertical scale ℓ_v, as listed in table 2. Both λ_{fgm} and ℓ_v decrease with a reduction in Fr, aligning with the expected scaling for layering induced by zigzag instabilities.

4. Concluding remarks

We investigated the dynamics of columnar Taylor–Green (TG) vortices under strong stratification ($Fr \leq 1.0$), with a particular focus on identifying and understanding the primary instabilities (§ 2) that lead to the breakdown of such vortices (§ 3). Our analysis revisited the instability mechanism of the most unstable eigenmode, identified

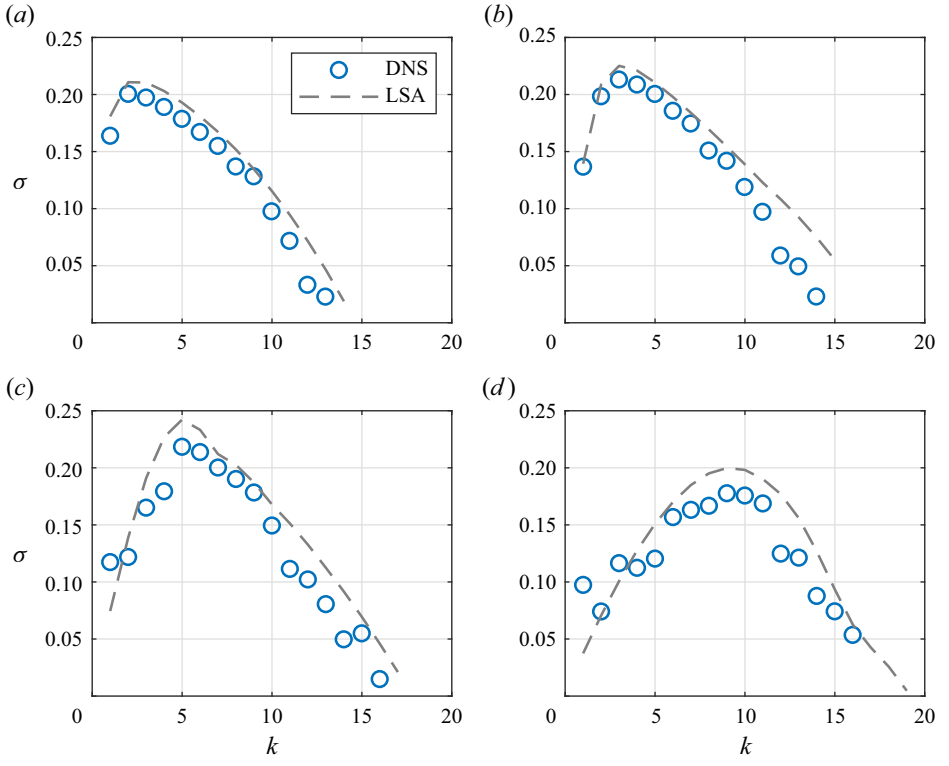

Figure 15. Comparison of the mode-by-mode growth rate $\sigma(k)$ estimated from DNS data with the prediction (figure 2) of the linear stability analysis (LSA) presented in § 2. Here, (*a*) $Fr = 1.0$, (*b*) $Fr = 0.5$, (*c*) $Fr = 0.25$ and (*d*) $Fr = 0.125$.

by Hattori *et al.* (2021) as the mixed hyperbolic (MH) mode. We discovered that for the range of parameters investigated, these MH modes exhibit fastest-growing wavenumbers that are inversely proportional to Fr and an approximately constant dimensionless growth rate (§ 2.2), similar to the zigzag instability (Billant & Chomaz 2000*b*). A closer look at the eigenmode (§ 2.3) revealed that the MH mode within the columnar TG vortices bears structural and dynamical resemblance to the zigzag instability, hinting at the zigzag mechanism's broader relevance beyond its initial discovery in vortex pairs (dipoles). The DNS results presented in § 3 confirm that the zigzag-like linear instabilities are crucial in growing the initial perturbations to a finite amplitude, with the observed flow structure and growth rate aligning closely with the linear stability analysis. The dominance of the linear instabilities in the TG vortices contrasts with the non-normal, transient growth mechanism considered recently by Lewin & Caulfield (2024) for horizontally sheared stratified flows.

Our understanding of the zigzag instability originates from the pioneering work of Billant and Chomaz on vortex dipoles and the observed scaling $k \sim Fr^{-1}$. We have discovered that similar dynamics apply to vortex arrays, which implies that the zigzag mechanism is at least somewhat generic. Various DNS studies (e.g. Basak & Sarkar 2006; Brethouwer *et al.* 2007) have invoked the zigzag mechanism to explain the vertically non-uniform structures scaled by U_0/N. However, attributing the $k \sim Fr^{-1}$ scaling solely to zigzag instability may be premature, as the U_0/N scaling could arise from generic scaling arguments (Billant & Chomaz 2001) and not necessarily from one specific linear or nonlinear process.

This paper has focused on the linear aspects of zigzag instability in a vortex array. The exact path through which the primary zigzag instability transitions to secondary instabilities and subsequently to turbulence is highly interesting, and these nonlinear dynamics are the subjects of ongoing investigation. Given that zigzag instability can channel energy from large-scale horizontal vortical motions directly into vertical scales of U_0/N, this study's implications could extend to the understanding of energy pathways in stratified turbulence (Waite 2013), with potential applications in modelling geophysical flows and predicting energy transfers in various atmospheric and oceanic contexts. In such contexts, the Reynolds number is expected to be many orders of magnitude larger than the single Re value considered in this paper. Billant & Chomaz (2000*c*) demonstrated the variation of the peak growth rate with Re, and noted minimal impact of Re on the most unstable wavenumber k_{fgm}. Hattori *et al.* (2021) reported that a tenfold reduction in Re reduces growth rates at higher wavenumbers, likely due to increased viscous damping, with k_{fgm} remaining relatively constant with varying Re. Our analysis in § 2.2 reveals that zigzag modes are stabilized for $Fr < 0.125$ at $Re = 1600$, which prompts several questions. Could this lower bound of Fr for zigzag instability decrease further at higher Re values? How might a large Re alter the capacity of zigzag instability to initiate secondary instabilities and transition to turbulence at very low Fr values? Is there a connection between zigzag instability and the layered anisotropic stratified turbulence (LAST) regime (Caulfield 2021), and if so, how could one rigorously establish the dynamical path from the generic linear instability (e.g. zigzag) to the layered and potentially self-organized (see e.g. Zhou 2022) state that characterizes the LAST regime? These inquiries await answers as our ability to perform large-Re simulations advances with time.

Acknowledgements. Q.Z. would like to thank the Isaac Newton Institute for Mathematical Sciences, Cambridge, for support and hospitality during the programme 'Anti-diffusive dynamics: from sub-cellular to astrophysical scales', where work on this paper was undertaken.

Funding. The programme was funded by EPSRC grant EP/R014604/1. This work was partially supported by a grant from the Simons Foundation. J.G. and Q.Z. received support from a Discovery Grant provided by the Natural Sciences and Engineering Research Council (NSERC) of Canada. Computational efforts were facilitated by the Digital Research Alliance of Canada.

Declaration of interests. The authors report no conflict of interest.

Author ORCIDs.
Junwei Guo https://orcid.org/0000-0002-4724-9810;
John R. Taylor https://orcid.org/0000-0002-1292-3756;
Qi Zhou https://orcid.org/0000-0002-7731-0360.

Appendix A. Formulation of the eigenvalue problem

Linearizing the momentum equation (2.5*a*) for the 2-D base flow (2.7) yields

$$\partial_t u + A_u = -\partial_x p + Re^{-1}\,\nabla^2 u, \tag{A1a}$$

$$\partial_t v + A_v = -\partial_y p + Re^{-1}\,\nabla^2 v, \tag{A1b}$$

$$\partial_t w + A_w = -\partial_z p + Re^{-1}\,\nabla^2 w - Fr^{-2}\,\rho, \tag{A1c}$$

where the advection terms are

$$A_u = (\partial_x U + U\,\partial_x + V\,\partial_y)u + v\,\partial_y U, \tag{A2a}$$

$$A_v = (\partial_y V + U\,\partial_x + V\,\partial_y)v + u\,\partial_x V, \tag{A2b}$$

$$A_w = (U\,\partial_x + V\,\partial_y)w, \tag{A2c}$$

respectively. Taking the divergence of (A1) yields

$$\partial_x A_u + \partial_y A_v + \partial_z A_w = -\Delta p - Fr^{-2}\,\partial_z \rho, \tag{A3}$$

where $\Delta \equiv \nabla^2$ is the Laplacian operator. Introducing

$$\mathcal{F} \equiv -\Delta p = \partial_x A_u + \partial_y A_v + \partial_z A_w + Fr^{-2}\,\partial_z \rho, \tag{A4}$$

and taking the Laplacians of (A1*a*) and (A1*b*), respectively, the horizontal momentum equations can be rewritten as

$$\partial_t \Delta u + \Delta A_u = \partial_x \Delta \mathcal{F} + Re^{-1}\,\Delta(\Delta u), \tag{A5a}$$

$$\partial_t \Delta v + \Delta A_v = \partial_y \Delta \mathcal{F} + Re^{-1}\,\Delta(\Delta v). \tag{A5b}$$

The linearized density equation (2.5*c*) reads

$$\partial_t \rho + (U\,\partial_x + V\,\partial_y)\rho - w = (Re\,Pr)^{-1}\Delta\rho. \tag{A6}$$

Dropping all $\hat{\cdot}$ for the remainder of this appendix, and applying continuity to the ansatz (2.9), one obtains (for $k \neq 0$),

$$w = -(\mathrm{i}k)^{-1}(\partial_x u + \partial_y v), \tag{A7}$$

which can then be substituted into (A2*c*) and (A6) to eliminate w, while keeping (u, v, ρ) in the linear system. Substituting the ansatz (2.9) into (A5) and (A6) yields

$$\begin{aligned}\sigma\,\Delta u &= -\Delta A_u + \partial_x \mathcal{F} + Re^{-1}\,\Delta^2 u \\ &= -\Delta A_u + \partial_{xx} A_u + \partial_{xy} A_v + (\mathrm{i}k)\,\partial_x A_w \\ &\quad + Fr^{-2}\,(\mathrm{i}k)\,\partial_x \rho + Re^{-1}\,\Delta^2 u,\end{aligned} \tag{A8a}$$

$$\begin{aligned}\sigma\,\Delta v &= -\Delta A_v + \partial_y \mathcal{F} + Re^{-1}\,\Delta^2 v \\ &= -\Delta A_v + \partial_{yy} A_v + \partial_{yx} A_u + (\mathrm{i}k)\,\partial_y A_w \\ &\quad + Fr^{-2}\,(\mathrm{i}k)\,\partial_y \rho + Re^{-1}\,\Delta^2 v,\end{aligned} \tag{A8b}$$

$$\begin{aligned}\sigma\rho &= -(U\,\partial_x + V\,\partial_y)\rho - (\mathrm{i}k)^{-1}(\partial_x u + \partial_y v) \\ &\quad + (Re\,Pr)^{-1}\Delta\rho.\end{aligned} \tag{A8c}$$

Assembling the above linear equations in (u, v, ρ) in the matrix form yields the generalized eigenvalue problem expressed in (2.10) in § 2.1.

Appendix B. The LB flow solver

The LB method offers a robust and efficient approach to solving the Navier–Stokes equations. In § 3, we adopted the 'OpenLB' code (Krause *et al.* 2020) to simulate density-stratified flows under the Boussinesq approximation (see full details in

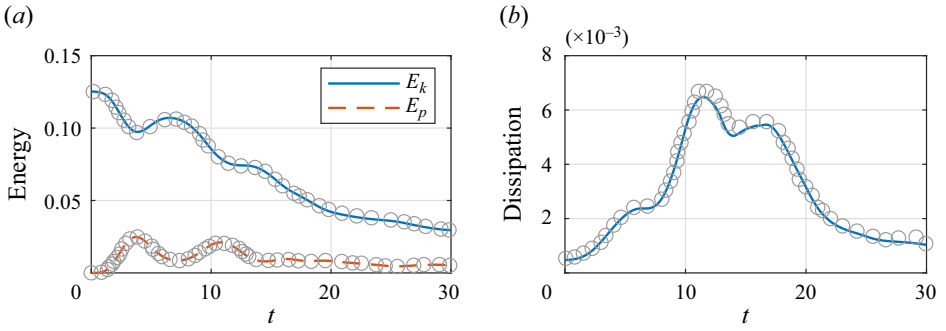

Figure 16. Time series of (*a*) E_k and E_p, and (*b*) $\varepsilon_k + \varepsilon_p$. The pseudo-spectral results by Jadhav & Chandy (2021) are plotted using circles, and the LB results using lines.

Guo *et al.* 2023). The LB solver advances the buoyancy and velocity fields in time through discrete lattice models and employing the Bhatnagar–Gross–Krook (BGK) collision operator. For the buoyancy field, the solver utilizes a D3Q7 lattice, where the buoyancy distribution functions are updated using the LB equation with a BGK collision operator. This operator allows the buoyancy distribution to relax towards an equilibrium state defined by the local buoyancy, fluid velocity and lattice weights, over a characteristic time scale set by the diffusivity of buoyancy. This process captures the advection and diffusion of buoyancy within the fluid. For the velocity field, a D3Q27 lattice is used in the present study, following the recommendation of Wilde *et al.* (2023). The LB equation for velocity includes both the standard BGK collision operator and an additional source term representing the buoyancy force. The BGK operator here ensures the relaxation of the velocity distribution towards its equilibrium over a time scale set by the fluid's viscosity, and the source term provides the dynamical coupling from buoyancy to velocity.

Guo *et al.* (2023) validated the LB solver's accuracy for a stratified, doubly periodic, wall-driven turbulent flow. Additional validation is performed as a part of the present study for a triply periodic flow under the 3-D TG configuration studied by Riley & de Bruyn Kops (2003). Specifically, the initial flow field for the validation case has a z-dependence:

$$(U, V, W) = (\sin x \cos y \cos z, -\cos x \sin y \cos z, 0). \tag{B1}$$

The flow parameters were set to $(Re, Fr, Pr) = (1600, 1.0, 0.7)$ for comparison with the DNS data from Jadhav & Chandy (2021), who used a conventional pseudo-spectral solver with a 512^3 grid, and applied the $2/3$ truncation rule for dealiasing. The LB simulation was conducted on a 252^3 grid, achieving resolution up to approximately 1.6 times the Kolmogorov scale at peak dissipation. Figure 16 compares the evolution of turbulent kinetic energy E_k and potential energy E_p, along with the sum of their dissipation rates, $\varepsilon_k + \varepsilon_p$, where

$$\varepsilon_k = \frac{1}{Re}\left\langle \frac{\partial u_i}{\partial x_j}\frac{\partial u_i}{\partial x_j}\right\rangle, \quad \varepsilon_p = \frac{1}{Re\,Pr\,Fr^2}\left\langle \frac{\partial \rho}{\partial x_i}\frac{\partial \rho}{\partial x_i}\right\rangle. \tag{B2a,b}$$

The comparison suggests good agreement between the pseudo-spectral and LB results.

References

Arobone, E. & Sarkar, S. 2012 Evolution of a stratified rotating shear layer with horizontal shear. Part I. Linear stability. *J. Fluid Mech.* **703**, 29–48.

AUGIER, P. & BILLANT, P. 2011 Onset of secondary instabilities on the zigzag instability in stratified fluids. *J. Fluid Mech.* **682**, 120–131.

AUGIER, P., CHOMAZ, J.-M. & BILLANT, P. 2012 Spectral analysis of the transition to turbulence from a dipole in stratified fluid. *J. Fluid Mech.* **713**, 86–108.

BASAK, S. & SARKAR, S. 2006 Dynamics of a stratified shear layer with horizontal shear. *J. Fluid Mech.* **568**, 19–54.

BILLANT, P. & CHOMAZ, J.-M. 2000*a* Experimental evidence for a new instability of a vertical columnar vortex pair in a strongly stratified fluid. *J. Fluid Mech.* **418**, 167–188.

BILLANT, P. & CHOMAZ, J.-M. 2000*b* Theoretical analysis of the zigzag instability of a vertical columnar vortex pair in a strongly stratified fluid. *J. Fluid Mech.* **419**, 29–63.

BILLANT, P. & CHOMAZ, J.-M. 2000*c* Three-dimensional stability of a vertical columnar vortex pair in a stratified fluid. *J. Fluid Mech.* **419**, 65–91.

BILLANT, P. & CHOMAZ, J.-M. 2001 Self-similarity of strongly stratified inviscid flows. *Phys. Fluids* **13**, 1645.

BRETHOUWER, G., BILLANT, P., LINDBORG, E. & CHOMAZ, J.-M. 2007 Scaling analysis and simulation of strongly stratified turbulent flows. *J. Fluid Mech.* **585**, 343–368.

CAULFIELD, C.P. 2021 Layering, instabilities, and mixing in turbulent stratified flows. *Ann. Rev. Fluid Mech.* **53**, 113–145.

CHOMAZ, J.-M. 2018 A flow on the verge of turbulent breakdown. *J. Fluid Mech.* **854**, 1–4.

DELONCLE, A., BILLANT, P. & CHOMAZ, J.-M. 2008 Nonlinear evolution of the zigzag instability in stratified fluids: a shortcut on the route to dissipation. *J. Fluid Mech.* **599**, 229–239.

DELONCLE, A., BILLANT, P. & CHOMAZ, J.-M. 2011 Three-dimensional stability of vortex arrays in a stratified and rotating fluid. *J. Fluid Mech.* **678**, 482–510.

DELONCLE, A., CHOMAZ, J.-M. & BILLANT, P. 2007 Three-dimensional stability of a horizontally sheared flow in a stably stratified fluid. *J. Fluid Mech.* **570**, 297–305.

DRITSCHEL, D.G. & DE LA TORRE JUÁREZ, M. 1996 The instability and breakdown of tall columnar vortices in a quasi-geostrophic fluid. *J. Fluid Mech.* **328**, 129–160.

GUO, J., ZHOU, Q. & WONG, R.C.-K. 2023 Direct simulation of stably stratified wall-bounded turbulence using the lattice Boltzmann method. *Phys. Fluids* **35**, 045151.

HATTORI, Y. & HIROTA, M. 2023 Stability of two-dimensional Taylor–Green vortices in rotating stratified fluids. *J. Fluid Mech.* **967**, A32.

HATTORI, Y., SUZUKI, S., HIROTA, M. & KHANDELWAL, M. 2021 Modal stability analysis of arrays of stably stratified vortices. *J. Fluid Mech.* **909**, A4.

HOLFORD, J.M. & LINDEN, P.F. 1999 Turbulent mixing in a stratified fluid. *Dyn. Atmos. Ocean* **30**, 173–198.

HOWLAND, C.J., TAYLOR, J.R. & CAULFIELD, C.P. 2020 Mixing in forced stratified turbulence and its dependence on large-scale forcing. *J. Fluid Mech.* **898**, A7.

JADHAV, K. & CHANDY, A.J. 2021 Assessment of SGS models for large eddy simulation (LES) of a stratified Taylor–Green vortex. *Flow Turbul. Combust.* **106**, 37–60.

KIM, J. & MOIN, P. 1985 Application of a fractional-step method to incompressible Navier–Stokes equations. *J. Comput. Phys.* **59**, 308–323.

KRAUSE, M.J., *et al.* 2020 OpenLB – open source lattice Boltzmann code. *Comput. Math. Appl.* **81**, 258–288.

LEBLANC, S. & GODEFERD, F.S. 1999 An illustration of the link between ribs and hyperbolic instability. *Phys. Fluids* **11**, 497–499.

LEFAUVE, A., PARTRIDGE, J.L., ZHOU, Q., DALZIEL, S.B., CAULFIELD, C.P. & LINDEN, P.F. 2018 The structure and origin of confined Holmboe waves. *J. Fluid Mech.* **848**, 508–544.

LEWIN, S.F. & CAULFIELD, C.P. 2024 Evidence for layered anisotropic stratified turbulence in a freely evolving horizontal shear flow. *J. Fluid Mech.* **983**, A20.

LUCAS, D., CAULFIELD, C.P. & KERSWELL, R.R. 2017 Layer formation in horizontally forced stratified turbulence: connecting exact coherent structures to linear instabilities. *J. Fluid Mech.* **832**, 409–437.

MAFFIOLI, A. & DAVIDSON, P.A. 2016 Dynamics of stratified turbulence decaying from a high buoyancy Reynolds number. *J. Fluid Mech.* **786**, 210–233.

OTHEGUY, P., CHOMAZ, J.-M. & BILLANT, P. 2006 Elliptic and zigzag instabilities on co-rotating vertical vortices in a stratified fluid. *J. Fluid Mech.* **553**, 253–272.

POTYLITSIN, P.G. & PELTIER, W.R. 1998 Stratification effects on the stability of columnar vortices on the f-plane. *J. Fluid Mech.* **355**, 45–79.

PRAUD, O., FINCHAM, A.M. & SOMMERIA, J. 2005 Decaying grid turbulence in a strongly stratified fluid. *J. Fluid Mech.* **522**, 1–33.

RILEY, J.J. & DE BRUYN KOPS, S.M. 2003 Dynamics of turbulence strongly influenced by buoyancy. *Phys. Fluids* **15**, 2047.

SPEDDING, G.R. 2014 Wake signature detection. *Ann. Rev. Fluid Mech.* **46**, 273–302.
SUZUKI, S., HIROTA, M. & HATTORI, Y. 2018 Strato-hyperbolic instability: a new mechanism of instability in stably stratified vortices. *J. Fluid Mech.* **854**, 293–323.
TAYLOR, G.I. & GREEN, A.E. 1937 Mechanism of the production of small eddies from large ones. *Proc. R. Soc. Lond.* A **158**, 499–521.
WAITE, M.L. 2013 The vortex instability pathway in stratified turbulence. *J. Fluid Mech.* **716**, 1–4.
WAITE, M.L. & BARTELLO, P. 2004 Stratified turbulence dominated by vortical motion. *J. Fluid Mech.* **517**, 281–308.
WAITE, M.L. & SMOLARKIEWICZ, P.K. 2008 Instability and breakdown of a vertical vortex pair in a strongly stratified fluid. *J. Fluid Mech.* **606**, 239–273.
WEIDEMAN, J.A. & REDDY, S.C. 2000 A MATLAB differentiation matrix suite. *ACM Trans. Math. Softw.* **26**, 465–519.
WILDE, D., NIDHAN, S., PHAM, H.T., FOYSI, H., REITH, D. & SARKAR, S. 2023 Stratified Taylor–Green vortex by lattice Boltzmann methods: influence of stencils, forcing schemes, and collision models. *Comput. Fluids* **256**, 105838.
ZHOU, Q. 2022 Threshold behavior of local gradient Richardson number in strongly stratified nonequilibrium turbulence. *Phys. Rev. Fluids* **7**, 104802.
ZHOU, Q. & DIAMESSIS, P.J. 2019 Large-scale characteristics of stratified wake turbulence at varying Reynolds number. *Phys. Rev. Fluids* **4**, 084802.